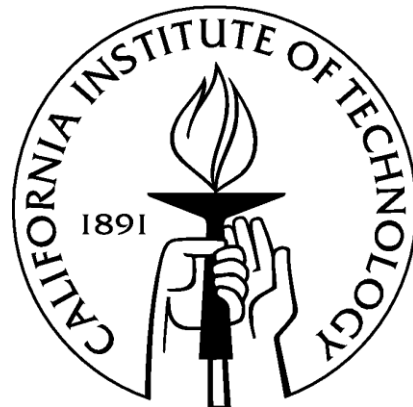


DEVELOPING AND CHARACTERIZING BULK METALLIC GLASSES
FOR EXTREME APPLICATIONS

THESIS BY

SCOTT NOLAN ROBERTS

IN PARTIAL FULFILLMENT OF THE REQUIREMENTS FOR THE DEGREE OF
DOCTOR OF PHILOSOPHY



CALIFORNIA INSTITUTE OF TECHNOLOGY

PASADENA, CALIFORNIA

2014

DEFENDED DECEMBER 16, 2013

© 2013

SCOTT ROBERTS

ALL RIGHTS RESERVED

NOTHING IS TOO SMALL...

PUT DOWN IN RECORD EVEN YOUR DOUBTS AND SURMISES...

WE LEARN FROM FAILURE,

NOT FROM SUCCESS!

ABRAHAM VAN HELSING, M.D., D.PH., D.LITT., ETC.

ABSTRACT

Metallic glasses have typically been treated as a “one size fits all” type of material. Every alloy is considered to have high strength, high hardness, large elastic limits, corrosion resistance, etc. However, similar to traditional crystalline materials, properties are strongly dependent upon the constituent elements, how it was processed, and the conditions under which it will be used. An important distinction which can be made is between metallic glasses and their composites. Charpy impact toughness measurements are performed to determine the effect processing and microstructure have on bulk metallic glass matrix composites (BMGMCs). Samples are suction cast, machined from commercial plates, and semi-solidly forged (SSF). The SSF specimens have been found to have the highest impact toughness due to the coarsening of the dendrites, which occurs during the semi-solid processing stages. Ductile to brittle transition (DTBT) temperatures are measured for a BMGMC. While at room temperature the BMGMC is highly toughened compared to a fully glassy alloy, it undergoes a DTBT by 250 K. At this point, its impact toughness mirrors that of the constituent glassy matrix. In the following chapter, BMGMCs are shown to have the capability of being capacitively welded to form single, monolithic structures. Shear measurements are performed across welded samples, and, at sufficient weld energies, are found to retain the strength of the parent alloy. Cross-sections are inspected via SEM and no visible crystallization of the matrix occurs.

Next, metallic glasses and BMGMCs are formed into sheets and eggbox structures are tested in hypervelocity impacts. Metallic glasses are ideal candidates for protection against micrometeorite orbital debris due to their high hardness and relatively low density. A flat single layer, flat BMG is compared to a BMGMC eggbox and the latter creates a more diffuse projectile cloud after penetration. A three tiered eggbox structure is also tested by firing a 3.17 mm

aluminum sphere at 2.7 km/s at it. The projectile penetrates the first two layers, but is successfully contained by the third.

A large series of metallic glass alloys are created and their wear loss is measured in a pin on disk test. Wear is found to vary dramatically among different metallic glasses, with some considerably outperforming the current state-of-the-art crystalline material (most notably $\text{Cu}_{43}\text{Zr}_{43}\text{Al}_7\text{Be}_7$). Others, on the other hand, suffered extensive wear loss. Commercially available Vitreloy 1 lost nearly three times as much mass in wear as alloy prepared in a laboratory setting. No conclusive correlations can be found between any set of mechanical properties (hardness, density, elastic, bulk, or shear modulus, Poisson's ratio, frictional force, and run in time) and wear loss. Heat treatments are performed on Vitreloy 1 and $\text{Cu}_{43}\text{Zr}_{43}\text{Al}_7\text{Be}_7$. Anneals near the glass transition temperature are found to increase hardness slightly, but decrease wear loss significantly. Crystallization of both alloys leads to dramatic increases in wear resistance. Finally, wear tests under vacuum are performed on the two alloys above. Vitreloy 1 experiences a dramatic decrease in wear loss, while $\text{Cu}_{43}\text{Zr}_{43}\text{Al}_7\text{Be}_7$ has a moderate increase. Meanwhile, gears are fabricated through three techniques: electrical discharge machining of 1 cm by 3 mm cylinders, semisolid forging, and copper mold suction casting. Initial testing finds the pin on disk test to be an accurate predictor of wear performance in gears.

The final chapter explores an exciting technique in the field of additive manufacturing. Laser engineered net shaping (LENS) is a method whereby small amounts of metallic powders are melted by a laser such that shapes and designs can be built layer by layer into a final part. The technique is extended to mixing different powders during melting, so that compositional gradients can be created across a manufactured part. Two compositional gradients are fabricated and characterized. Ti-6Al-4V to pure vanadium was chosen for its combination of high

strength and light weight on one end, and high melting point on the other. It was inspected by cross-sectional x-ray diffraction, and only the anticipated phases were present. 304L stainless steel to Invar 36 was created in both pillar and as a radial gradient. It combines strength and weldability along with a zero coefficient of thermal expansion material. Only the austenite phase is found to be present via x-ray diffraction. Coefficient of thermal expansion is measured for four compositions, and it is found to be tunable depending on composition.

ACKNOWLEDGEMENTS

First, I would like to thank my advisor, Bill Johnson. Back when I was doing graduate school interviews, I remember Bill was the first professor I interviewed with. An hour later, I felt torn. If every professor was as excited about their work as Bill, how would I ever choose where to attend school? After visiting a few more schools the choice was obvious. I would be attending Caltech. When I started in the lab in the fall of 2007, Aaron Wiest taught me the ropes and helped guide me through my candidacy project.

After Aaron graduated, I found myself working with Doug Hofmann on semisolid forging of metallic glass composites. Doug continued as a mentor to me throughout my graduate career, and I look forward to working with him in the future in our lab at the Jet Propulsion Laboratory.

I'd also like to thank all of my fellow labmates. Henry Kozachkov for always being a sympathetic ear and being able to make me laugh harder than anyone else. Joanna Kolodziejska for all her help with my later projects, and being willing to actually get stuff done when the rest of us were at the point of giving up. Andrew Hoff for being continually eager to learn about everything we've been doing in the lab, and help rekindle my passion for what I had been doing throughout my graduate career. Xiao Lu for saving my bacon a number of times when I was TAing APh 105. Dale Conner for our many discussions on research possibilities. It's a shame our melt spinner had to meet the fate it did. Marios Demetriou for always keeping group meeting interesting.

My classmates at Caltech were also a continual source of inspiration. The first two years here were some of the hardest of my life, and I wouldn't have been able to get through without

my study group: Aaron Varga, Nick Stadie, Chatr Panithipongwut, Jorge Munoz, and Pratyush Tiwary. During my time here at Caltech, I've also spent a lot of time TAing classes. Thank you to everyone that attended recitations, asked questions, and helped me make the best of nine terms of teaching assistant duties. The ISP lunches hosted by Daniel Yoder and Laura Flower Kim offered a weekly chance to kick back, enjoy some good food, and learn about my colleagues from all over the world. Their sponsoring of the summer softball team, the Asteroid Pirates, I co-captained with Lisa Mauger also gave a lot of us a fun way of getting some sun.

Finally, I'd like to thank all those closest to me. My parents have always done their best to stand by my decisions and support me throughout my struggles. It didn't matter if it was standing up for my argument with a teacher on displaying my artwork in elementary school or moving 3000 miles from home to attend grad school. Last, but certainly not least, is my partner through this long journey, Sanda Cea. Her faith in my ability to finish my degree at Caltech even prior to my acceptance here has helped me stay positive time and time again. There's no way I would have been able to finish my thesis without the many nights you kept me company in the office while I battled my way through this document. If you ever decide to write a thesis yourself, I'll have to find a bigger couch.

TABLE OF CONTENTS

TABLE OF CONTENTS	ix
LIST OF FIGURES	x
LIST OF TABLES	xv
CHAPTER 1 - INTRODUCTION	1
CHAPTER 2 - EFFECTS OF PROCESSING AND TEMPERATURE ON CHARPY IMPACT TOUGHNESS IN METALLIC GLASSES AND METALLIC GLASS MATRIX COMPOSITES	17
CHAPTER 3 - CAPACITIVE JOINING AND ASSEMBLY OF BULK METALLIC GLASS MATRIX COMPOSITES	47
CHAPTER 4 - METALLIC GLASSES AS SHIELDING FOR HYPERVELOCITY IMPACTS	59
CHAPTER 5 - WEAR BEHAVIOR OF METALLIC GLASS GEARS	73
CHAPTER 6 - CHARACTERIZATION OF TWO GRADIENT ALLOYS FABRICATED BY LASER ENGINEERED NET SHAPING	115
APPENDIX A - COMPLETE TABLE OF MEASURED PROPERTIES FOR WEAR TESTING	133
APPENDIX B - A SERIES OF OTHER STUDIES PERFORMED	137

LIST OF FIGURES

FIGURE 1-1: (A) A SHEAR BAND BEGINNING TO GROW IN A BMG. (B) FAILURE BY A SINGLE SHEAR BAND IN A BULK GLASS. (C) MULTIPLE SHEAR BANDS GROWTH BEING ARRESTED BY A SECONDARY PHASE.	3
Figure 2-1: Geometry required for an ASTM standard Charpy impact test. ¹ Type A is the geometry modified for our testing due to limitation in casting thickness in BMG alloys.....	18
Figure 2-2: A schematic of a Charpy impact test. ²	19
Figure 2-3: Instrumented small-scale Charpy testing. (a) The pendulum hammer has been stripped of excess mass to reduce the impact energy. A plastic extension has been built to hold the magnet. As the pendulum swings, the magnet passes a coil before and after impact, which registers a current. (b) The modified sample holder has a shorter span length of 20 mm for compact Charpy samples. (c) Suction cast (SC) samples of the alloy DV1. (d) Induced current obtained from an impact test on DH3 using a digital oscilloscope. The hammer's speed is reduced during impact, which broadens the second peak. The width of the coils and magnets are known to be $dx = 1$ cm, so the velocity of the hammer can be determined through $v = dx/dt$. The energy during the impact is $E = 1/2 mv^2$	24
Figure 2-4: The temperature calibration curve for DH3 ($Zr_{39.9}Ti_{33.9}Nb_{7.6}Cu_{6.4}Be_{12.5}$).	25
Figure 2-5: Compact Charpy impact toughness values from 11 alloys tested; one bulk metallic glass (BMG), six bulk metallic glass matrix composites (DH3, DV1, LM2) in various processing conditions, and four crystalline alloys. The processing conditions are commercially cast plate (CCP), crystalline (xtal), suction cast (SC), and semisolidly forged (SSF). The maximum hammer energy for the low drop height is displayed on the plot along with a scaled estimation of the full-sized Charpy toughness. On average, seven samples of each alloy were tested, and the average is plotted as a red circle.....	28
Figure 2-6: Fracture surfaces from six BMGMC samples tested in this study, along with their impact energy. X-ray scans from SSF DH3 and the completely crystalline state are also shown. Although the body-centered cubic dendrites remain in the crystalline sample, the matrix is no longer amorphous, as evident from the numerous starred peaks. Also shown are magnified fracture surfaces from SSF, DH3, and LM2, showing the difference in the fracture pattern. All images are of the fracture surface taken with backscattered electrons in a SEM.	30
Figure 2-7: (a) A backscattered SEM micrograph showing a fractured specimen of commercially cast LM2. Despite the large, coarse dendrites, other factors (like oxygen content and partial crystallization) make this the most brittle alloy tested. (b) The edge of the crack from a region in (a) demonstrating very little toughness. (c) Another region near the edge of the crack showing that several shear bands have formed. (d) A region where the matrix has crystallized into an unknown brittle phase.	31
Figure 2-8: Backscattered SEM micrographs from the BMGMC DV1 (40% dendrite). (a) Crack originating at the notch and then propagating through a SSF sample during a compact Charpy test. (b),(c) Higher magnification of shear bands interacting with the Ti-based dendrites (e) Crack propagating through a SC sample during compact Charpy test. (e),(h) Higher magnification micrographs of shear bands in the SC sample along with the nominal microstructure.	33
Figure 2-9: (a) Crack arrest and branching after impact in a SSF sample. (b) Near the edge of the crack, many shear bands have formed and been arrested by the soft dendrites. (c) Magnification of a region in (a) demonstrating that even far away from the crack, shear bands still form in the glass matrix. (e) Crack propagating through a SC sample of DH3 and (f),(g) higher magnification images of the shear bands and microstructure.	35
Figure 2-10: Charpy impact toughness vs. temperature for pure Sn and the BMG Vitreloy 1 compared with data obtained from References ¹⁹ and ⁴ . The plot shows that the compact impact setup used in this	

work recreates the correct DTBT temperature in Sn and reproduces the shape of the curves from literature, despite the smaller specimen size. An estimate of the full-sized Charpy toughness is shown on the right axis. All the data is shown.....	38
Figure 2-11: Charpy impact toughness vs. temperature for the BMGMC DH3 and its glass matrix, made separately. The curves represent the averages all of the data, which are also shown. Both alloys were produced via suction casting and notched identically.....	38
Figure 2-12: (a-c) SEM micrographs from the surface of polished Charpy specimens in the BMGMC DH3 showing how the crack morphology changes with temperature. (a) 300K, (b) 163 K, and (c) 100 K. (d-e) Enlarged micrographs of the shear bands on the surface of the DH3 sample impacted at room temperature. Similar images are shown for cryogenic specimens, (f) 163 K and (g) 100 K.	41
Figure 2-13: (a) SEM micrograph of the fracture surface from the monolithic BMG DH3-Matrix impacted at 300K. (b) DH3-Matrix 100 K. (c) Fracture surface from BMGMC DH3 at 100 K. In all samples the notch is at the bottom of the images.....	42
FIGURE 3-1: (A) MAXIMUM SHEAR STRESS VERSUS WELDING POWER FOR PLATES OF THE BMGMC DH1 THAT WERE SUBJECTED TO FOUR WELDS FOR EACH POWER. THE SCHEMATIC SHOWS THAT THE GEOMETRY OF THE PLATES WAS DESIGNED SO THAT THE TENSION TEST APPLIES PURE SHEAR TO THE WELDED REGIONS. THE RED SOLID CIRCLES REPRESENT FAILURE IN THE WELDS WHILE THE FILLED BLUE CIRCLES REPRESENT FAILURE OUTSIDE THE WELDED REGION. (B-C) EXAMPLES OF HOW COPPER ELECTRODES CAN BE BENT TO DO “PROJECTION WELDING.” IN THIS CASE, A SQUARE HONEYCOMB OF THE BMGMC DH1 IS WELDED TOGETHER FROM CORRUGATED STRIPS. (D) A TRUSS WELDED FABRICATED BY WELDING TOGETHER 1 MM DIAMETER RODS OF THE BMGMC DH1 AT THE NODES.....	50
FIGURE 3-2: (A) AN OPTICAL IMAGE OF THE NODES BETWEEN TWO WELDED DH1 EGG-BOXES SHOWING THE EXTENT OF FLOW DURING THE WELDING. (B-E) PROGRESSIVELY ENLARGED SEM MICROGRAPHS SHOWING THE MICROSTRUCTURE OF THE WELDED REGIONS. THE LOW MAGNIFICATION MICROGRAPH IN (B) SHOWS THE THAT MATERIAL HAS FLOWED FROM UNDER THE WELDING ELECTRODES. AT HIGHER MAGNIFICATION (C) THERE IS A CLEAR SEAM BETWEEN THE TWO WELDED PIECES THAT DISAPPEARS IN THE LOCATION UNDER THE ELECTRODES, INDICATING A SOLID WELD. (D-E) ENLARGEMENTS OF THE WELD REGION SHOWING FLOW LINES FROM THE JOINING BUT ALSO SHOWING DENDRITES THAT WERE UNAFFECTED BY THE FLOWING GLASS MATRIX. THE WELD IS COMPRISED ON THE GLASS MATRIX FROM EACH SAMPLE HAVING BEEN HEATED AND JOINED UNDER THE COMPRESSIVE LOADS WITHOUT THE DENDRITES BEING AFFECTED. THE DENDRITE MICROSTRUCTURES IN (D-E) ARE NOMINAL FOR THE SAMPLE OUTSIDE THE WELDED REGION.	52
FIGURE 3-3: QUASISTATIC COMPRESSION TESTING OF TWO DH1 EGG-BOXES THAT WERE WELDED TOGETHER AT FIVE LOCATIONS. THE BLUE CURVE REPRESENTS A WELDING POWER OF 20 J (PICTURED ON TOP) WHILE THE RED CURVE REPRESENTS 40 J (PICTURED ON BOTTOM). UNDER COMPRESSION, THE SAMPLES EXPERIENCE A MIXED-MODE BUCKLING FROM EDGE EFFECTS WHICH ULTIMATELY BREAKS THE WELD. AT 40 J, THERE IS A SIGNIFICANT AMOUNT OF BUCKLING BEFORE THE WELD FAILS, INDICATING A HIGHER QUALITY WELD. THIS IS VERIFIED BY THE COMPRESSION DATA, WHICH SHOWS A HIGHER ENERGY ABSORPTION IN THE 40 J WELDED SAMPLES.....	54
FIGURE 4-1: A SCHEMATIC OF A WHIPPLE SHIELD WITH A FRONT BUMPER, EMPTY SPACE, AND A REAR WALL TO CATCH DEBRIS. (B) IMPACTS WILL CREATE A CLOUD OF DEBRIS BOTH FORWARDS AND BACKWARDS. (C) IF THE DEBRIS CLOUD IS NOT SUFFICIENTLY DIFFUSE IT CAN RESULT IN EITHER FURTHER PENETRATION OR DETACHED SPALL FROM THE REAR WALL. IMAGE FROM REFERENCE ⁵	61
FIGURE 4-2: HYPERVELOCITY FACILITY AND TEST SAMPLES – (A) VIEW OF THE NASA AMES VERTICAL GUN RANGE, WHICH CONSISTS OF A TWO-STAGE LIGHT GAS GUN CAPABLE OF FIRING PROJECTILES IN TWO DIFFERENT CONFIGURATIONS TO ALLOW SIMULATIONS OF IMPACTS FROM 0.8 TO 5.5 KM/S. THE ENVIRONMENTAL TEST CHAMBER IS OVER 2 M HIGH AND THE ANGLE OF IMPACT CAN BE CHANGED USING MULTIPLE PORTS ON THE SIDE. (B) FORGING CHAMBER USED TO FABRICATE THIN PLATES AND EGGBOX STRUCTURES. (C) EXAMPLE OF A 10 G INGOT OF THE BMGMC DH1 ($Zr_{36.6}Ti_{31.4}Nb_7Cu_{5.9}Be_{19.1}$) FORGED INTO A 0.8 MM THICK SHEET. (D) MOLD USED TO FORGE EGGBOX PANELS FROM BMGMCs. (E) BMGMC EGGBOX WITH A 0.6 MM THICK WALL SEMISOLIDLY FORGED AND THE NOMINAL	

MICROSTRUCTURE SHOWN IN THE INSET. (F) EGGBOX PANEL FIXED TO TESTING JIG. THE HOLE IN THE BOTTOM PLATE ALLOWS FOR THE COLLECTION OF DEBRIS FROM THE IMPACT. DURING SOME IMPACTS, A WITNESS PLATE WAS USED INSTEAD TO ASSESS DAMAGE. (G) SETUP OF THE HIGH-SPEED CAMERAS USED TO CAPTURE THE IMPACT. THREE CAMERAS CAN BE SEEN IN THE IMAGE (ONE IS AT THE UPPER RIGHT). ..	64
FIGURE 4-3: COMPARISON OF SURFACE GEOMETRY DURING HYPERVELOCITY IMPACTS IN BMG COMPOSITE PANELS. (A) BACKLIT SIDE-VIEW IMAGES FROM A 3.17 MM ALUMINUM SPHERE IMPACTING A 0.6 MM THICK DH1 EGGBOX, SHOWN IN (C), AT 2.7 KM/s FOR THE FIRST 102 μ s AFTER IMPACT. THE MULTI-FACETED SURFACE EFFECTIVELY DIFFUSES THE IMPACT INTO A BROAD DEBRIS CLOUD. (B) THE SAME VELOCITY IMPACT AS (A) INTO A 0.7 MM THICK BMGMC COMPOSITE SHEET. THE IMPACT CONDITIONS AND ALLOY ARE THE SAME BETWEEN (A) AND (B) BUT THE SURFACE GEOMETRY IS DIFFERENT. IN (B) THE DEBRIS CLOUD IS TIGHTLY CLUSTERED AFTER IMPACT. (C) PLOT OF LIGHT INTENSITY VERSUS FRAME NUMBER FOR THE HYPERVELOCITY TESTS IN (A,B). AS AN ESTIMATION OF ENERGY RELEASED DURING IMPACT, IMAGE ANALYSIS WAS USED TO DETERMINE THE LENGTH AND INTENSITY OF THE LIGHT. THE EGGBOX IS MUCH MORE EFFECTIVE THAN THE THIN SHEET AT DISSIPATING ENERGY. (D,E) IMAGE ANALYSIS WAS USED TO DESIGNATE A RANGE OF ANGLE OF THE DEBRIS CLOUD THAT CAPTURES AT LEAST 95% OF THE DEBRIS. THE EGGBOX GEOMETRY (D) HAS A 25° WIDER SPREAD THAN THE THIN SHEET (E). (F,G) LONG EXPOSURE IMAGES FROM THE IMPACTS IN THE EGGBOX (F) AND THE THIN SHEET (G) ILLUSTRATING THE DIFFERENCE IN LIGHT INTENSITY DURING THE IMPACT. THE RED LIGHT IS THE LASER USED TO TRIGGER THE HIGH-SPEED CAMERA.	66
FIGURE 4-4: HYPERVELOCITY IMPACT OF A WELDED BMG COMPOSITE CELLULAR STRUCTURE. (A) SCHEMATIC OF THE CAPACITIVE JOINING PROCESS FOR A BMG COMPOSITE. (B) SHAPED ELECTRONS ON A SPOT WELDER WERE USED TO WELD EGG-BOXES TOGETHER. (C) SEM MICROGRAPH FROM TWO EGG-BOX PANELS WELDED TOGETHER. (D-E) EGG-BOX PANELS WHICH HAVE BEEN WELDED TOGETHER. (F) ALUMINUM HSP STRUCTURE. (G) BACKLIT SIDE VIEW OF THE THREE LAYER EGG-BOX STRUCTURE BEING IMPACTED BY A 3.17 MM ALUMINUM PROJECTILE AT 2.3 KM s^{-1} SHOWING PENETRATION OF THE FIRST LAYER AND SLIGHT PENETRATION OF THE SECOND LAYER. (H) PLOT SHOWING PROJECTILE DIAMETER VERSUS PROJECTILE VELOCITY FOR ALUMINUM SANDWICH PANELS WITH ALUMINUM FACESHEETS CALCULATED FROM BALLISTIC LIMIT SOFTWARE. S IS THE HEIGHT OF THE HONEYCOMBS AND T IS THE THICKNESS OF THE FACE SHEETS. (I) THE LAYERED EGG-BOX STRUCTURE LOADED INTO THE SAMPLE HOLDER. (J) A LONG EXPOSURE IMAGE SHOWING THE LIGHT GENERATED DURING THE HYPERVELOCITY IMPACT.	68
FIGURE 5-1: COMMON WEAR TEST GEOMETRIES: (A) PIN-ON-DISC WITH CIRCULAR TRACK (B) PIN-ON-DISC WITH SPIRAL TRACK (C) PIN-ON-PLATE (D) BLOCK-ON-RING (E) DISC-ON-WHEEL (F) THRUST WASHER (G) BALL-ON-PRISM (H) FOUR BALL. PIN-ON-DISC AND PIN-ON-PLATE MAY BE IDENTIFIED AS BALL-ON-DISC OR BALL-ON-PLATE, RESPECTIVELY, IF THE PIN HAS A HEMISPHERICAL TIP. ⁸	74
FIGURE 5-2: A) A SCHEMATIC FOR A CYLINDER-ON-DISK TEST. B) HIGHLIGHTING THE MOUNTING SYSTEM FOR THE CYLINDER AND DEMONSTRATING THE LINE CONTACT. C) A CYLINDER-ON-DISK TEST IN PROGRESS.	79
FIGURE 5-3: PROFILOMETRY DATA FOR THREE SAMPLES. THE Ti-BASED COMPOSITE AND Zr-BASED AM WERE BOTH POLISHED TO A 0.02 μ M FINISH, WHILE THE NITRONIC 60 SAMPLE WAS FINISHED ON A LATHE. INSET ARE IMAGES OF EACH SAMPLE POST-WEAR.	81
FIGURE 5-4: A) A SCHEMATIC DIAGRAM OF THE ASTM STANDARD PIN-ON-DISK TEST. B) AN OVERHEAD VIEW OF A POD TEST IN PROGRESS. WEAR DEBRIS CAN BE SEEN ON THE EDGES OF THE SAMPLE HOLDER. C) AN OVERVIEW OF THE POD TESTER. THE PIN IS LOCATED AT THE END OF A LONG ARM TO ALLOW FOR PRECISE APPLICATION OF A NORMAL FORCE. D) AN AS-CAST SAMPLE PRIOR TO REMOVAL OF GATE MATERIAL.	83
FIGURE 5-5: A COMPARISON OF LINE PROFILES BETWEEN DIFFERENT ALLOYS AFTER A PIN-ON-DISK TEST. A LARGE DIFFERENCE CAN BE SEEN BETWEEN THE CURRENT GEAR MATERIAL, VASCOMAX, AND ONE OF THE WORST PERFORMING BMG ALLOYS TESTED.	88
FIGURE 5-6: MEASURING VOLUME LOSS BY PROFILOMETRY SEEMS TO CONSISTENTLY UNDERESTIMATE THE AMOUNT OF WEAR LOSS COMPARED TO MEASURING MASS CHANGES. ALLOYS ARE BOTH AMORPHOUS, COMPOSITES, AND CRYSTALLINE.	89

FIGURE 5-7: A) K VERSUS HARDNESS. THESE ARE TYPICALLY CONSIDERED DIRECTLY PROPORTIONAL, HOWEVER FOR OUR ALLOYS THERE SEEMS TO BE NO TREND. B) K VERSUS E/H . THE QUOTIENT OF ELASTIC MODULUS TO HARDNESS CAN BE SEEN AS A RATIO OF ELASTICITY VERSUS RESISTANCE TO PLASTIC DEFORMATION. C) AS EXPECTED, E IS FAIRLY PROPORTIONAL TO H_V . ALL ALLOYS ARE AMORPHOUS.....	90
FIGURE 5-8: K , THE DIMENSIONAL WEAR COEFFICIENT VERSUS EACH OF THE ELASTIC CONSTANTS. K IS IN UNITS $mm^3/(N\cdot m)$	92
FIGURE 5-9: A) A TYPICAL FRICTION VS TIME PLOT FROM THE ALLOY $Cu_{43}Zr_{43}Al_7Ag_7$. THE RED SECTION IS THE RUN-IN PERIOD, AT WHICH THERE IS LITTLE FRICTION DUE TO A LACK OF WEAR DEBRIS ALONG THE TRACK. THE GREEN REGION IS THE STEADY STATE REGION, AND WHERE THE AVERAGE FRICTION FORCE WAS MEASURED. B) K VERSUS AVERAGE FRICTION. C) K VS RUN IN TIME. D) RUN IN TIME VERSUS AVERAGE FRICTION. ONLY AMORPHOUS ALLOYS ARE SHOWN.....	93
FIGURE 5-10: WEAR LOSS AND HARDNESS DATA AFTER ANNEALING OF $Zr_{35}Ti_{30}Be_{27.5}Cu_{7.5}$	95
FIGURE 5-11: WEAR LOSS AND HARDNESS DATA AFTER ANNEALING OF $Cu_{43}Zr_{43}Al_7Be_7$	96
FIGURE 5-12: A) A MICROGRAPH OF DEBRIS ALONG THE WEAR TRACK OF CRYSTALLIZED $Cu_{43}Zr_{43}Al_7Be_7$. B) A QBSD MICROGRAPH OF THE WEAR TRACK. BRIGHTER SPOTS INDICATE HIGHER Z ELEMENTS. C) LOCATION SELECTED FOR EDS OF WEAR DEBRIS. D) LOTS OF IRON WAS FOUND IN THE WEAR TRACK, WHILE NONE WAS FOUND IN BULK AREAS OF THE SAMPLE (NOT SHOWN).	97
FIGURE 5-13: A COMPARISON OF WEAR COEFFICIENTS FOR TWO ALLOYS UNDER AIR AND VACUUM. THE $ZrTi$ ALLOY SEES NOTABLE IMPROVEMENTS, WHILE THE $CuZr$ ALLOY HAS DECREASE PERFORMANCE.....	100
FIGURE 5-14: A) THE SEMISOLID FORGING SETUP. B) A PREALLOYED BMGMC INGOT SET UP TO BE FORGED. C) A FINISHED COMPOSITE GEAR ONCE IT HAS BEEN REMOVED FROM THE MOLD. D) THE COMPLETED GEAR ONCE IT HAS HAD A HOLE DRILLED AND AXLE INSERTED. E) A PERSPECTIVE IMAGE SHOWING THE FINISH ON THE GEAR TEETH. F) A SEM MICROGRAPH WHERE SOME OF THE CASTING DEFECTS ARE VISIBLE.	102
FIGURE 5-15: A) THE GEAR MOLD FULLY ASSEMBLED WITHOUT THE CAP ON TOP. B) AN IMAGE A CAST GEAR STILL IN THE MOLD. UPPER GATE MATERIAL STILL CONNECTS TO THE POOL IT WAS CAST FROM. C) THE BOTTOM OF THE MOLD. D) GEAR ONCE IT HAS BEEN REMOVED FROM THE MOLD. E) LEFT, GEAR WITH A KEYWAY MACHINED OUT. RIGHT, A GEAR WITH FLASHING REMOVED AND FACES GROUNDED TO A $16\ \mu m$ FINISH.	103
FIGURE 5-16: THE GEAR TESTING MACHINE. KEY COMPONENTS ARE LABELED.	104
FIGURE 5-17: WEAR LOSS PER HOUR FOR EACH OF THE GEAR PAIRS TESTED.	105
FIGURE 5-18: TOP, APPEARANCE OF GEARS PRIOR TO TESTING. BOTTOM, EFFECTS OF WEARING ON EACH OF THE ALLOYS. THE ARROWS ON THE VASCOMAX IMAGE HIGHLIGHT THEIR WEAR.....	107
FIGURE 5-19: ABOVE: DARKFIELD IMAGES OF $CuZrAlBe$ AND UNCOATED VASCOMAX GEARS. SMALL AMOUNTS OF WEAR CAN BE SEEN ON THE LEFT SIDE OF THE TEETH FOR BOTH GEARS. BELOW: THE DIFFERENCE IN EDGE PROFILES BETWEEN UNWORN (BLACK) AND WORN (RED) GEARS.	108
FIGURE 6-1: SCHEMATIC OF THE LASER DEPOSITION (LD) BUILDING HEADS USED TO FABRICATE GRADIENT ALLOYS. (B) IMAGE OF THE LD PROCESS FABRICATING SEVERAL TEST SPECIMENS OF THE Ti-V GRADIENTS. (C) THREE GRADIENT ALLOY SPECIMENS; A HOLLOW CYLINDER, A PLATE AND A BEAM. (D) EXAMPLE OF A "FOREST" OF GRADIENT ALLOY POSTS USED TO VARY GRADIENT COMPOSITIONS.	117
FIGURE 6-2: (A) A BINARY Ti-V PHASE DIAGRAM. A IS HCP AND B IS BCC. (B) TERNARY Ti-Al-V PHASE DIAGRAM. THE ADDITION OF ALUMINUM TO THE SYSTEM APPEARS TO BROADEN THE TWO PHASE REGION SLIGHTLY. THE OUTLINED PATH DEMONSTRATES THE COMPOSITIONS CONTAINED IN THE TESTED PILLAR. ^{6,7}	120
FIGURE 6-3: (A) A HARDNESS VS POSITION PLOT FOR THE Ti-6-4 TO V SAMPLE. (B) 3D MAPPING OF XRD INTENSITIES ACROSS THE SAMPLE. A SLOW CHANGE IN DIFFRACTION ANGLES IS APPARENT IN THE BCC PHASE. (C) INDEXED DIFFRACTION PATTERNS IDENTIFIED TO IN (A). THE COEXISTANCE OF BOTH HCP AND BCC PHASES IS DEMONSTRATED.....	121
FIGURE 6-4: VOLUME OF A UNIT CELL VERSUS COMPOSITION. AS MORE TITANIUM IS ADDED, AN INCREASE IN CELL VOLUME CAN BE SEEN. BETA-TITANIUM HAS A LARGER LATTICE CONSTANT THAN VANADIUM ($3.282\ \text{\AA}$ FOR Ti VERSUS $3.020\ \text{\AA}$ FOR V), SO THIS EXPANSION IS REASONABLE.....	123

FIGURE 6-5: (A) SCHEMATIC OF THE ROTATIONAL DEPOSITION PROCESS USED TO DEVELOP ALLOYS WITH GRADIENT COMPOSITIONS IN A RADIAL DIRECTION. (B) IMAGE OF TWO RADIALLY GROWN ALLOYS WHERE A 304L TO INVAR 36 GRADIENT WAS APPLIED TO A ROTATING A286 STAINLESS STEEL ROD. (C) A CALCULATED PHASE DIAGRAM AT 923 K SHOWING THE GRADIENT PATH FROM 304L TO INVAR 36. PHASE DIAGRAM CALCULATED BY OUR COLLABORATOR, RICHARD OTIS FROM PENN STATE.....	124
FIGURE 6-6: (A) PRINTED AND MACHINED INSERTS FOR CARBON FIBER AND ALUMINUM HONEYCOMB SHEETS. (B) AN INSERT INSTALLED INTO A PANEL. (C) BEFORE AND AFTER A PULL-OUT TEST.....	126
FIGURE 6-7: X-RAY SCANS WERE OBTAINED FOR THE RADIAL SAMPLE AS WELL AS FOR THE LINEAR SAMPLE OF 304L TO INVAR 36. THE RADIAL ALLOY WAS SECTIONED ACCORDING TO THE MAP ABOVE AND X-RAY SCANS WERE PERFORMED ON EACH SECTION, SHOWN AT RIGHT. ONLY THE AUSTENITE PHASE WAS DETECTED.....	127
FIGURE 6-8: (A) A REPRESENTATIVE THERMAL EXPANSION MEASUREMENT PLOTTING PROBE POSITION VS. TEMPERATURE. THE FIRST CYCLE WAS ALWAYS DISCARDED SINCE IT WAS USED TO "SEAT" THE SAMPLE PROPERLY UNDER THE LOAD. (B) EXPANSION OF THE CYLINDER VERSUS TEMPERATURE. FOUR OF THOSE MEASUREMENTS ARE SHOWN, ONE FROM THE INVAR SIDE OF THE GRADIENT, ONE FROM THE STEEL SIDE, AND TWO SAMPLES NEAR THE INVAR SIDE OF THE GRADIENT. SAMPLE 2 REPRESENTS THE SAMPLE MOST NEAR THE PURE INVAR, AND SAMPLE 3 IS THE NEXT SAMPLE BEYOND THAT. (C) THE CTE WAS OBTAINED BY DIFFERENTIATING THE CURVES FROM (B).....	128

LIST OF TABLES

TABLE 2-1: PHYSICAL & MECHANICAL PROPERTIES OF SAMPLES MEASURED VIA CHARPY IMPACT TESTING.	26
TABLE 2-2: SUMMARY OF DH3 DTBT IMPACTS.....	44
TABLE 4-1: BALLISTIC LIMIT EQUATIONS FOR VARIOUS MATERIALS	62
TABLE 5-1: SUMMARY OF PIN-ON-DISK RESULTS	80
TABLE 6-1: BUILD CONDITIONS FOR THE Ti-6Al-4V GRADIENT ALLOY.....	118
TABLE 6-2: LINEARIZED CTEs AND CHANGE IN CTE FROM AMBIENT TEMPERATURES TO 373 K.....	130
TABLE A-1: COMPLETE TABLE OF MEASURED PROPERTIES FOR WEAR TESTING	133